Identification of Fenton-like active Cu sites by heteroatom modulation of electronic density

Xiao Zhou[a,b,1], Ming-Kun Ke (柯明坤)[c,1], Gui-Xiang Huang[c], Cai Chen[b], Wenxing Chen[d], Kuang Liang[b], Yunteng Qu[b], Jia Yang[b], Ying Wang[a,2], Fengting Li[a], Han-Qing Yu[c,2], and Yuen Wu[b,e,2]

[a]College of Environmental Science and Engineering, Tongji University, State Key Laboratory of Pollution Control and Resources Reuse, Shanghai 200092, China; [b]Hefei National Laboratory for Physical Sciences at the Microscale, School of Chemistry and Materials Science, University of Science and Technology of China, Hefei 230026, China; [c]Chinese Academy of Sciences Key Laboratory of Urban Pollutant Conversion, Department of Environmental Science and Engineering, University of Science and Technology of China, Hefei 230026, China; [d]Beijing Key Laboratory of Construction Tailorable Advanced Functional Materials and Green Applications, School of Materials Science and Engineering, Beijing Institute of Technology, Beijing 100081, China; and [e]Dalian National Laboratory for Clean Energy, Dalian 116023, China

Edited by Alexis Bell, Department of Chemical and Biomolecular Engineering, University of California, Berkeley, CA; received October 25, 2021; accepted December 15, 2021

Developing heterogeneous catalysts with atomically dispersed active sites is vital to boost peroxymonosulfate (PMS) activation for Fenton-like activity, but how to controllably adjust the electronic configuration of metal centers to further improve the activation kinetics still remains a great challenge. Herein, we report a systematic investigation into heteroatom-doped engineering for tuning the electronic structure of Cu-N_4 sites by integrating electron-deficient boron (B) or electron-rich phosphorus (P) heteroatoms into carbon substrate for PMS activation. The electron-depleted Cu-N_4/C-B is found to exhibit the most active oxidation capacity among the prepared Cu-N_4 single-atom catalysts, which is at the top rankings of the Cu-based catalysts and is superior to most of the state-of-the-art heterogeneous Fenton-like catalysts. Conversely, the electron-enriched Cu-N_4/C-P induces a decrease in PMS activation. Both experimental results and theoretical simulations unravel that the long-range interaction with B atoms decreases the electronic density of Cu active sites and down-shifts the d-band center, and thereby optimizes the adsorption energy for PMS activation. This study provides an approach to finely control the electronic structure of Cu-N_4 sites at the atomic level and is expected to guide the design of smart Fenton-like catalysts.

single-atom catalysts | electronic structure | heteroatom-doped engineering | reaction kinetics | Fenton-like process

The Fenton-like process presents one of the most powerful water treatment technologies to tackle persistent organic pollutants resulting from rapid economic development and unsustainable industrial and agricultural expansion (1–4). The peroxymonosulfate (PMS)-based advanced oxidation process has attracted extensive attention due to its high efficiency at a wide pH range and ease of transport and storage (5–7). However, the sluggish kinetics of PMS activation during oxidation processes results in prohibitive costs and substantial chemical inputs (8, 9). Therefore, developing efficient catalysts to accelerate the reaction kinetics of PMS is crucial toward efficient catalytic oxidation of recalcitrant organics. Although homogeneous first-row transition metals (Co^{2+}, Fe^{2+}, Cu^{2+}, and Mn^{2+}) generally exhibit remarkable capabilities for PMS activation, they also suffer problems such as poor recyclability and accumulation of sludge (10–12). Comparatively, heterogeneous catalysts [e.g., transition metal oxides (13, 14), supported nanoparticles (NPs) (15, 16), and carbon-based materials (17, 18)] can be readily recovered and regenerated and are recognized as promising candidates for PMS activation. Nevertheless, the heterogeneity of NPs results in lower utilization efficiency of surface atoms (with 81.6% atoms buried and unavailable for 6-nm nickel NPs) and generally slower reaction kinetics than their homogeneous counterparts (19).

Single-atom catalysts (SACs) featuring utmost atom-utilization efficiency and tunable electronic structure can break the limitations of heterogeneous catalysts in terms of the kinetics and catalytic activity (20, 21). Thus, SACs show a great potential to address the slow reaction kinetics of PMS for the Fenton-like process via maximizing the number of catalytic sites (22). For instance, a single-site Fe catalyst exhibited much faster reaction kinetics toward the degradation of phenol than the Fe NP catalyst, owing to the maximized atomic utilization (23). In addition, the synergetic effect between the atomic center and pyrrolic N site of supports endowed Co SACs with dual reaction sites and high activity for PMS-based oxidation (24). To further accelerate the reaction kinetics of PMS, various strategies have been developed to improve the intrinsic activity of single atomic sites. By controlling the configurations of single atomic sites, PMS was more favorable for adsorption and activation on the CoN_{2+2} site than the CoN_4 site (25). Previous work shows that manipulating the electronic structure of single sites plays an essential role in mediating the intrinsic activity (26, 27). It is highly desirable to gain insights into tuning the electronic structure of single-atom sites to achieve superior PMS activation kinetics.

Significance

The Fenton-like process based on peroxymonosulfate (PMS) has been widely investigated and recognized as a promising alternative in recent years for the degradation of persistent organic pollutants. However, the sluggish kinetics of PMS activation results in prohibitive costs and substantial chemical inputs, impeding its practical applications in water purification. This work demonstrates that tuning the electronic structure of single-atom sites at the atomic level is a powerful approach to achieve superior PMS activation kinetics. The Cu-based catalyst with the optimized electronic structure exhibits superior performance over most of the state-of-the-art heterogeneous Fenton-like catalysts, while homogeneous Cu(II) shows very poor activity. This work provides insights into the electronic structure regulation of metal centers and structure–activity relationship at the atomic level.

Author contributions: Y. Wang, H.-Q.Y., and Y. Wu designed research; X.Z. and M.-K.K. performed research; G.-X.H., C.C., K.L., and J.Y. contributed new reagents/analytic tools; X.Z., M.-K.K., W.C., Y.Q., and F.L. analyzed data; and X.Z., Y. Wang, H.-Q.Y., and Y. Wu wrote the paper.

The authors declare no competing interest.

This article is a PNAS Direct Submission.

[1]X.Z. and M-K.K. contributed equally to this work.

[2]To whom correspondence may be addressed. Email: yingwang@tongji.edu.cn, hqyu@ustc.edu.cn, or yuenwu@ustc.edu.cn.

This article contains supporting information online at http://www.pnas.org/lookup/suppl/doi:10.1073/pnas.2119492119/-/DCSupplemental.

Published February 14, 2022.

Recent studies demonstrate that the electronic structure of isolated metal sites can be directly modulated by altering the coordinated atom species of the metal centers, favorable for expediting catalytic activity (28, 29). Notably, controlling the long-range interactions with suitable functionalities on the substrate of SACs can be a promising approach for tuning the electronic structure of metal centers (30). Indeed, the kinetic activity of single atomic sites was successfully tuned by the introduction of electron-withdrawing oxidized S groups or electron-donating thiophene-like S species into carbon supports of SACs (31). To this end, nonmetallic heteroatoms offer a substantial potential to serve as electron-withdrawing/donating functionalities on the carbon plane by chemical substitution (32, 33). Specifically, boron (B) with a vacant $2p_z$ orbital conjugating with the carbon π system extracts the electrons, while phosphorus (P) with a readily available lone electron pair and low electronegativity is expected to donate electron in graphene (34, 35). With this strategy, incorporating particular heteroatoms (B/P) into the substrate is a possible route to deplete/enrich the electronic density of metal centers, tuning the electronic structure of single sites to promote PMS activation kinetics.

In this work, we designed a versatile strategy to systematically tune the electronic structure of Cu-N_4 sites by integrating specific heteroatoms (B/P) into N-doped carbon substrates of Cu SACs. Subsequently, the effect of the controlled electronic features of Cu centers on facilitating PMS reaction kinetics was explored. Here, the heteroatom modified Cu-N_4 catalysts were first prepared by using a hydrogen-bonding-assisted pyrolysis approach. Synchrotron X-ray adsorption spectroscopy and the projected density of states (PDOS) analysis verified the successful regulation of the electronic configuration of the Cu-N_4 SACs by different heteroatom functionalities. Furthermore, electron paramagnetic resonance and Raman spectra were employed to elucidate the PMS activation mechanism in the Cu-N_4/C-B/PMS system. This study opens an avenue to regulating the electronic structures of single active site of SACs to accelerate PMS activation kinetics for pollutant degradation.

Results and Discussion

Heteroatom-Doped Engineering of Cu SACs. Single-atom Cu catalysts decorated with specific nonmetallic heteroatom (Cu-N_4/C-B and Cu-N_4/C-P) were prepared through an H-bonding-assisted pyrolysis strategy to study the electronic structure effect of single Cu sites for PMS activation, as illustrated in Fig. 1*A*. Typically, boric/phosphoric acid and carbamide were adopted as building units for self-assembled architecture by H-bonding interaction. The Cu-contained precursor was homogeneously mixed with the supramolecular assembly. SACs consisting of Cu-N_4 active sites anchored on heteroatom substituted carbon supports were obtained after pyrolyzing the mixed powder under an Ar atmosphere. The control sample (denoted as Cu-N_4/C) without heteroatom was also prepared through a similar procedure but with some modifications (see *Materials and Methods*).

The transmission electron microscopy (TEM) images illustrate that Cu-N_4/C-B displays a thin graphene-like layered structure, without obvious agglomerates of Cu nanoparticles (*SI Appendix*, Fig. S1 *A* and *B*). As revealed by *SI Appendix*, Fig. S1*D*, the ring-like selected-area electron diffraction (SAED) pattern of Cu-N_4/C-B excludes the existence of crystalline Cu. The energy-dispersive spectroscopy (EDS) mapping images from Fig. 1*B* show that Cu, B, N, and C are distributed uniformly across the entire architecture. To investigate the dispersion properties of Cu species at the atomic level, the aberration-corrected high-angle dark-field scanning TEM (AC HAADF-STEM) measurement was carried out. As shown in Fig. 1 *C* and *D* and *SI Appendix*, Fig. S2, the single bright dots corresponding to isolated Cu atoms can be clearly distinguished from the heteroatom-doped carbon matrix. The atomic dispersion of Cu in Cu-N_4/C-B is further confirmed by the atom-overlapping Gaussian-function fitting mapping and analysis of intensity profile (Fig. 1*E*). The morphologies of Cu-N_4/C and Cu-N_4/C-P were also checked, revealing a similar thin graphene-like layered structure (*SI Appendix*, Figs. S3*A* and S4*A*). Additionally, the EDS mappings of Cu-N_4/C-P reveal the presence of Cu, C, N, and P elements (*SI Appendix*, Fig. S4 *C–F*).

The powder X-ray diffraction pattern of Cu-N_4/C-B exhibits only one broad peak at approximately 25° indexed to the (002) plane of the graphitic carbon (36), which is similar to these of Cu-N_4/C and Cu-N_4/C-P (*SI Appendix*, Fig. S5). No typical peaks ascribed to crystalline Cu species are observed, which is consistent with the observation from the SAED pattern. Moreover, the Raman spectra of the Cu-N_4 catalysts reveal the characteristic D and G bands of conductive carbon materials with similar calculated I_D/I_G values (*SI Appendix*, Fig. S6). Heteroatom modified SACs exhibit slightly larger values than the primary sample, indicating the formation of more defects and disordered structures in Cu-N_4/C-B and Cu-N_4/C-P. N_2 physisorption analysis confirms that all the catalysts have comparable BET surface areas and pore sizes (*SI Appendix*, Fig. S7). Furthermore, the Cu loadings, measured by inductively coupled plasma atomic emission spectroscopy, are close to each other in the Cu-N_4 catalysts (*SI Appendix*, Table S1). Considering all the above findings, there are no obvious differences in carbon crystallinity, surface area, or total Cu content for Cu-N_4/C, Cu-N_4/C-B, and Cu-N_4/C-P, which ensures that the effect of heteroatom decoration on the electronic structure of the Cu-N_4 catalysts could be investigated independently.

Atomic Structure and Chemical State Analysis of Cu SACs. Synchrotron X-ray absorption spectra were used to clarify the fine structures of Cu-N_4 catalysts. As shown in Fig. 2*A*, the Fourier transform extended X-ray absorption fine structure (FT-EXAFS) spectra of the Cu-N_4 catalysts all exhibit one major peak at about 1.5 Å, which can be attributed to Cu-N coordination (37). In contrast to Cu foil and CuO, the absence of a metallic Cu-Cu scattering path (2.2 Å) in the spectra of Cu-N_4 catalysts further verifies the atomic dispersion of Cu. To better investigate the atomic configuration of Cu-N_4 catalysts, wavelet transform (WT) analysis was performed, which can provide powerful resolution in both R and k spaces and discriminate the backscattering atoms. In line with the FT-EXAFS analysis, the WT contour plots of Cu-N_4 catalysts exhibit only one intensity maximum at 4.8 $Å^{-1}$, which is assigned to the Cu-N bond (Fig. 2 *G–I*). For comparison, both Cu foil and CuO counterparts show higher intensity maxima at 7.6 and 6.8 $Å^{-1}$, corresponding to Cu-Cu and Cu-O-Cu coordination, respectively (Fig. 2 *E* and *F*). We performed EXAFS fitting to analyze the structural parameters of Cu atoms (*SI Appendix*, Fig. S8 *A–F*), and the corresponding parameters are listed in *SI Appendix*, Table S2. It is observed that the best-fit EXAFS results match quite well with the experiment spectra. Based on the results, Cu species in three single-atom samples exist as the form of isolated Cu-N_4 sites, as illustrated by the local atomic structure model (insets in *SI Appendix*, Fig. S8 *B*, *D*, and *F*). The above results strongly suggest that Cu atoms are atomically dispersed in Cu-N_4/C, Cu-N_4/C-B, and Cu-N_4/C-P, without the existence of metal-derived crystalline structures.

The electronic structure of the prepared catalysts was first probed by soft X-ray absorption near-edge structure (XANES) analysis. As revealed in Fig. 2*B*, the N K-edge spectra of Cu-N_4 catalysts are dominated by three well-resolved resonance peaks attributed to the pyridinic π* (N1), graphitic π* (N2), and C–N σ* (N3) transitions, respectively (38). Notably, the typical peaks of Cu-N_4 catalyst shift to lower energy with P incorporation.

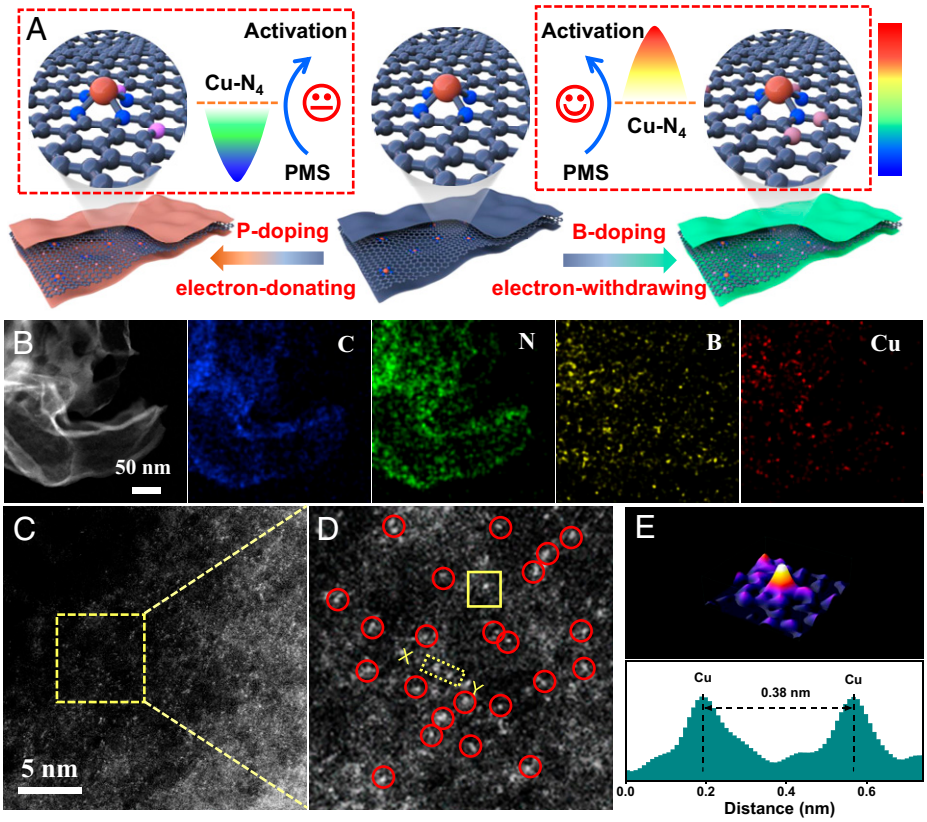

Fig. 1. Synthetic illustration and morphology characterizations. (*A*) Schematic of the preparation strategy for Cu-N_4/C-B and Cu-N_4/C-P. The color bar indicates the electronic density of Cu-N_4 site, electro-rich (blue) and electro-poor (red). (*B*) HAADF-STEM image and the corresponding EDS mapping images of Cu-N_4/C-B. (*C*) AC HAADF-STEM image and (*D*) enlarged intensity image of Cu-N_4/C-B. (*E*) Atom-overlapping Gaussian-function-fitting mapping of the square from *D*, intensity profile along X–Y in *D*.

A similar shift, but in the opposite direction (i.e., to higher energy), was observed in the case of B-decorated Cu-N_4 catalyst. The observed changes in the soft XANES spectra indicate a variation in the chemical environment around nitrogen atoms upon heteroatom doping (39, 40), strongly implying a possible change of electronic structure of Cu metal centers. Meanwhile, the B and P K-edge spectra confirm that heteroatoms (B/P) have been successfully doped into carbon substrate (*SI Appendix*, Fig. S9).

The Cu K-edge XANES spectra of Cu-N_4 catalysts were employed to survey the chemical state of Cu. The energy absorption thresholds of the three Cu-N_4 catalysts are situated between that of Cu foil and CuO, indicating the atomically dispersed Cu atoms carry partially positive charges (Fig. 2*C*). Of particular note is that the valence state of single Cu sites was found to rank in the order 2 > Cu-N_4/C-B > Cu-N_4/C > Cu-N_4/C-*P* > 0, which means the electronic properties of the Cu-N_4 sites can be tailored by controlling the heteroatom species in carbon substrate. This observation also shows a good agreement with the Cu 2*p* high-resolution X-ray photon spectroscopy (XPS) spectra. As shown in Fig. 2*D*, the fitted ratios of Cu (0) to Cu (2+) valence state in three Cu-N_4 catalysts show the same trend as the Cu K-edge XANES results, indicating that Cu-N_4/C-B possesses a higher chemical valence compared with Cu-N_4/C and Cu-N_4/C-P. Moreover, N 1*s* XPS spectra of Cu-N_4 catalysts exhibit three characteristic peaks derived from pyridinic N, pyrrolic N, and graphitic N, respectively (*SI Appendix*, Fig. S11) (41, 42). These N species exhibit different composition distributions and consequently are associated with the heteroatom incorporation. The successful modification of Cu-N_4 catalysts by heteroatoms was further confirmed by B 1*s* and P 2*p* XPS spectra of Cu-N_4/C-B and Cu-N_4/C-P, respectively.

Regulation of Cu Electronic Structure for PMS Activation. To assess the effect of heteroatom-induced electronic structure regulation of Cu centers on tuning PMS activation activity, the Fenton-like catalytic performance was evaluated for bisphenol A (BPA) removal. As shown in Fig. 3*A*, the pristine Cu-N_4/C catalyst achieved less than 60% degradation of BPA in 5 min. Remarkably, the electron-depleted Cu-N_4 sites drastically boosted the activation of PMS, with BPA almost completely decomposed using Cu-N_4/C-B as the catalyst. However, only about 11% BPA was degraded by PMS when Cu-N_4/C-P with electron-enriched Cu centers was employed. In order to provide a better comparison of the catalytic performance, the BPA removal kinetics were then fitted by the pseudo-first-order reactions. It is worth mentioning that the apparent rate constant (k) of Cu-N_4/C-B was ~70 and 5.5 times that of Cu-N_4/C-P and Cu-N_4/C, respectively (Fig. 3*B*), being one of the most active Cu-based catalysts for PMS activation (*SI Appendix*, Fig. S18 and Table S3). Homogeneous Cu catalyst [Cu(II)] showed very poor activity for the activation of PMS (*SI Appendix*, Fig. S20). Furthermore, the Fenton-like performance of Cu-N_4/C-B is superior to most of the state-of-the-art heterogeneous catalysts (*SI Appendix*, Fig. S19 and Table S4). In addition, the comparison with the BPA degradation kinetic curve of BCN without Cu active centers reveals that the Fenton-like activity was mainly ascribed to Cu-N_4 sites (Fig. 3*C*).

The dynamic enhancement in the oxidation performance of Cu-N_4/C-B indicates the critical role of electronic structure of Cu sites for catalytic PMS activation. Specifically, the reaction rate constant for the synthesized Cu-N_4 catalysts was found to correlate well with the Cu valence state calculated from XPS results (Fig. 3*D*). The B modified Cu SACs with a relatively

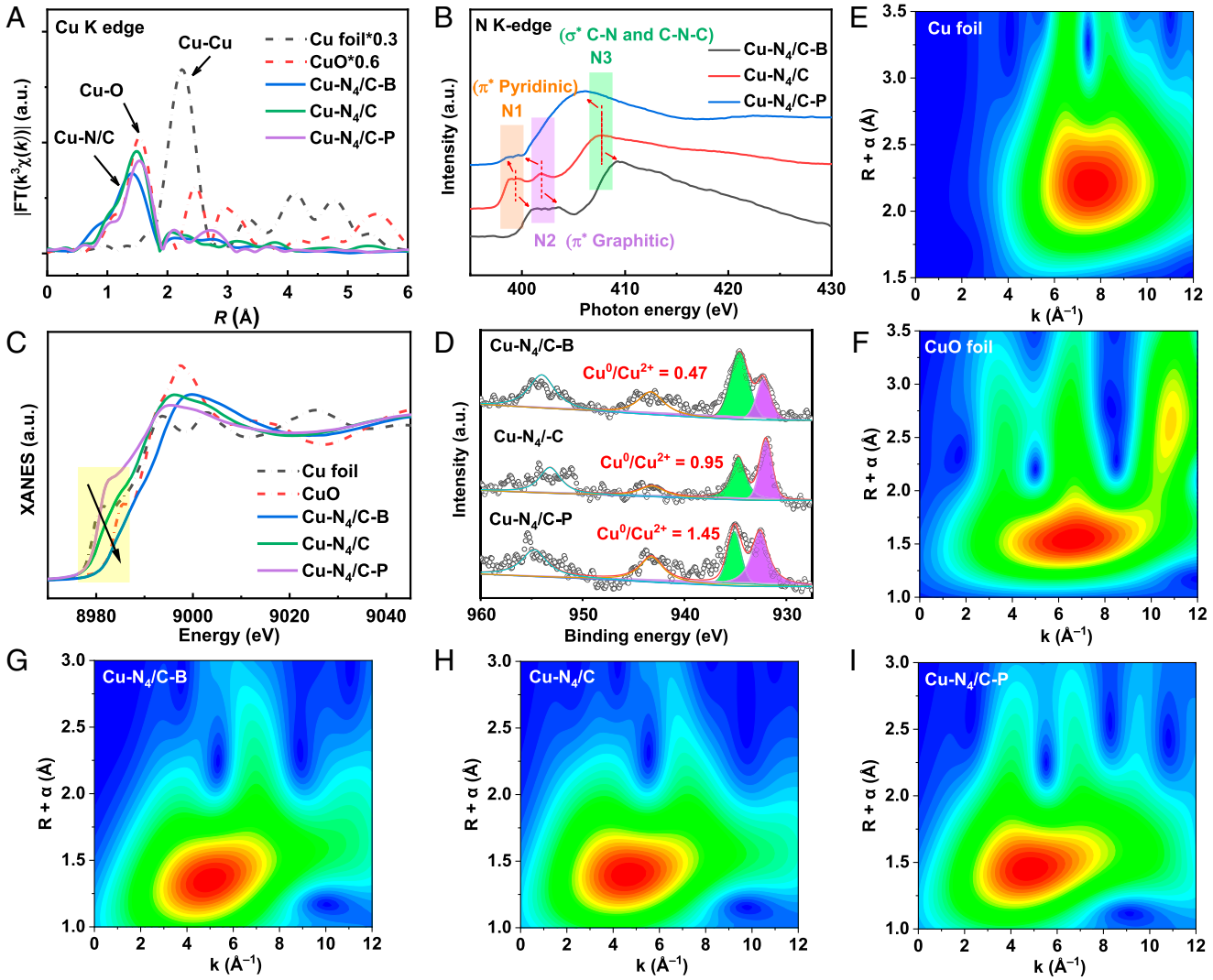

Fig. 2. Atomic local structure and chemical state of Cu-N_4 catalysts. (*A*) Cu K-edge FT-EXAFS spectra of Cu-N_4/C-B, Cu-N_4/C-P, Cu-N_4/C, and reference samples. (*B*) N K-edge XANES spectra of the Cu-N_4 catalysts. (*C*) The normalized Cu K-edge XANES spectra of the Cu-N_4 catalysts and the references (Cu foil and CuO). (*D*) Cu 2*p* XPS spectra of Cu-N_4/C-B, Cu-N_4/C-P, and Cu-N_4/C. (*E–I*) WT-EXAFS plots of Cu foil, CuO, Cu-N_4/C-B, Cu-N_4/C, and Cu-N_4/C-P, respectively.

high valence state led to a higher value of k in BPA removal. Cu-N_4/C-B catalyst with optimal B content showed the best activity for pollutant oxidation. However, the incorporation of P heteroatom into the substrates of Cu SACs enriched the electronic density of Cu centers (relatively low valence state), resulting in loss of degradation activity. In this regard, electronic structure regulation of metal centers can be an approach to enhance PMS activation kinetics. Moreover, Cu-N_4/C-B exhibited satisfying catalytic performance over a broad pH range (Fig. 3*E*), which is beneficial for practical treatment of wastewater.

To identify the reactive oxygen species (ROS) generated during PMS activation, electron paramagnetic resonance (EPR) experiments were conducted. As shown in Fig. 3*F*, the signals for the hydroxyl radical ($HO^{\bullet}$) and sulfate radical ($SO_4^{\bullet-}$) were barely detectable in the Cu-N_4/C-B/PMS system. Specifically, the characteristic triplet signals of TMP-$^1O_2$ adducts for the three Cu-N_4 catalysts exhibited enhanced intensity compared to PMS (*SI Appendix*, Fig. S24), implying the existence of singlet oxygen ($^1O_2$) during PMS activation (43). The EPR analysis suggested that the nonradical ROS was the dominant oxidant in the Cu-N_4/C-B/PMS system. Radical quenching experiments were carried out to further identify the active species during PMS activation. As shown in Fig. 3*G*, excessive ethanol (EtOH) served as radical scavengers for $SO_4^{\bullet-}$/$^{\bullet}OH$ (18, 44), with slight inhibition on BPA removal, indicating that both $SO_4^{\bullet-}$ and $^{\bullet}OH$ contributed little to BPA degradation. Both benzoquinone (BQ) and sodium azide (NaN_3) demonstrated noticeable inhibition effect on BPA degradation, suggesting the potential role of $^1O_2$ (45, 46). However, the solvent exchange (H_2O to D_2O) did not result in an acceleration of BPA decomposition (*SI Appendix*, Fig. S26*A*). This contradicts the previous findings that D_2O is a promoter for singlet oxygenation because the lifetime of $^1O_2$ in D_2O is extended up to 10 times (47, 48). Thus, $^1O_2$ was not primarily responsible for BPA degradation under such conditions, indicating the existence of a secondary nonradical PMS activation pathway (49, 50).

In fact, BQ and NaN_3 can also be oxidized by the activated PMS complex via a nonradical pathway (17). Therefore, potassium dichromate ($K_2Cr_2O_7$) was alternatively employed as an electron scavenger to investigate the electron transfer process. BPA decomposition was barely inhibited in the Cu-N_4/C-B/PMS

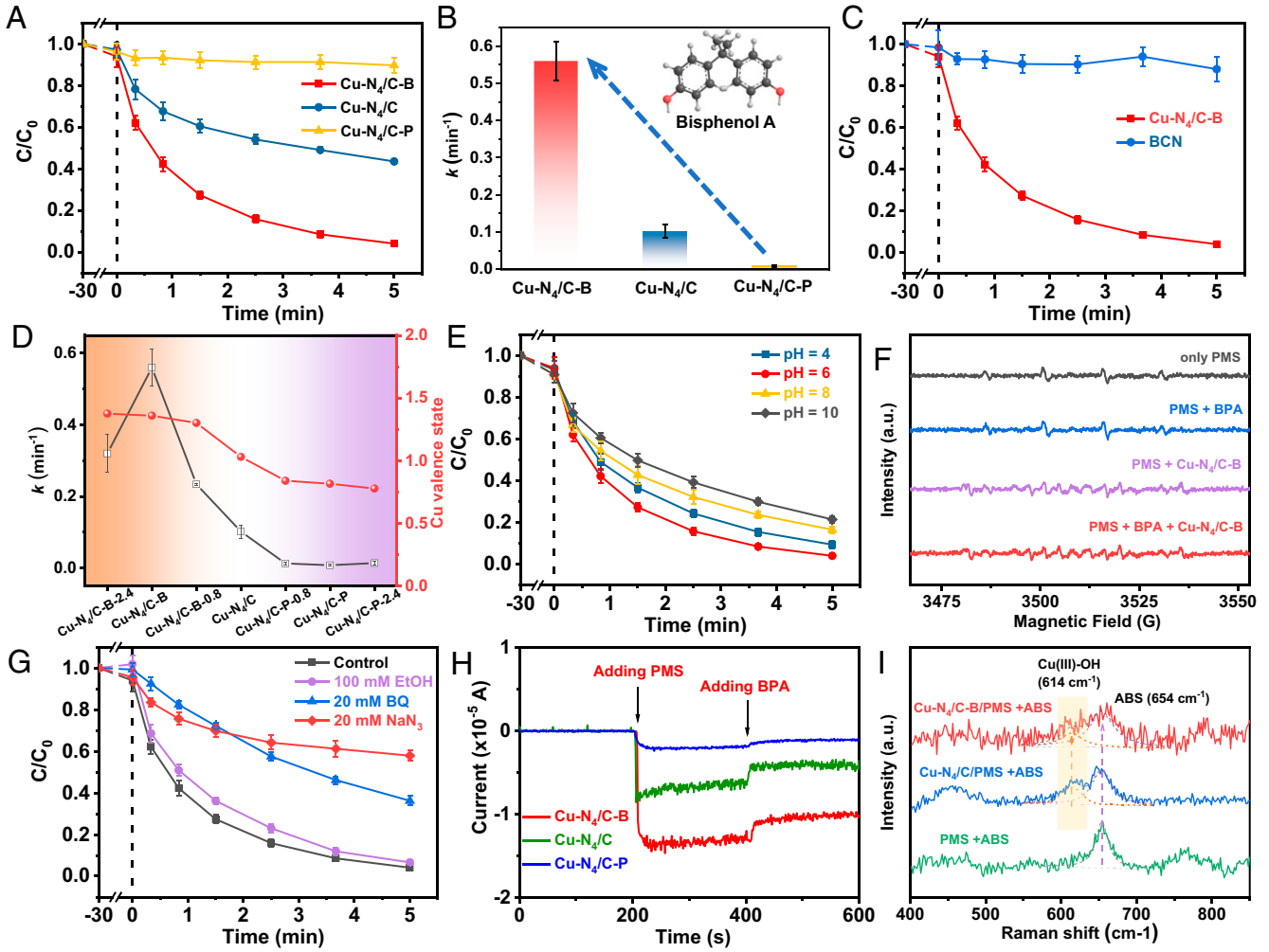

Fig. 3. Fenton-like performance for Cu-N_4 catalysts. (*A*) Kinetics of BPA degradation by PMS catalyzed by Cu-N_4/C-B, Cu-N_4/C, and Cu-N_4/C-P within 5 min. (*B*) Comparison of the rate constant of BPA removal by the three Cu-N_4 catalysts. (*C*) Kinetics of BPA degradation by PMS catalyzed by Cu-N_4/C-B and BCN. (*D*) The relationship between the rate constant and the Cu valence state in the prepared Cu-N_4 catalysts. (*E*) Influence of pH on BPA degradation in the Cu-N_4/C-B/PMS system. (*F*) EPR spectra in the activation of PMS in the presence of Cu-N_4/C-B catalyst. (*G*) Comparison of degradation kinetics under different quenching conditions. (*H*) Current responses after the sequential injection of PMS and BPA at the Cu-N_4/C-B, Cu-N_4/C, and Cu-N_4/C-P working electrodes. (*I*) Raman spectra of the Cu-N_4/C-B/PMS and Cu-N_4/C/PMS systems (ABS: pH buffer). Reaction condition: [BPA] = 20 mg·L^{-1}, [PMS] = 0.2 g·L^{-1}, catalyst = 0.1 g·L^{-1}, T = 298 K, initial solution pH = 6.0.

upon $K_2Cr_2O_7$ addition (*SI Appendix*, Fig. S26*B*), suggesting that the system was likely based on direct electron transfer on the catalyst surface other than in solution phase (51). Moreover, chronoamperometry measurements were performed (Fig. 3*H*) to verify PMS activation with Cu-N_4 catalysts. The injection of PMS caused distinct current jumps for the three Cu SACs, which verifies electron transfer in the Cu SACs/PMS systems and most likely from Cu SACs to PMS. Impressively, Cu-N_4/C-B exhibited the maximum intensity of current jump, demonstrating efficient electron transfer between Cu-N_4/C-B and PMS. It is well documented that high-valent intermediates are formed through heterolytically cleaving the peroxide O–O bond for transition metal catalyzed systems (52, 53). In this case, after electron transfer from Cu-N_4/C-B to PMS, high-valent copper-oxo species [Cu(III)-OH] were generated by heterolytic cleavage of the O–O bond and served as key intermediates in PMS activation. Furthermore, the subsequent injection of BPA led to the opposite direction of current change, implying electron transfer from BPA to Cu SACs, which resulted in BPA degradation.

To further verify the formation of high-valent copper during the PMS activation, Raman spectra were collected. As shown in Fig. 3*I*, the new peak around 614 cm^{-1} in the Cu-N_4/C-B/PMS system was likely due to high-valent copper-oxo species, because this is a characteristic Cu–O stretching vibration band of a metastable Cu(III) (7, 54). Moreover, this featured peak for Cu(III)-OH was also observed in the Cu-N_4/C/PMS system, further confirming the presence of high-valent copper intermediate during PMS activation. The peak at 654 cm^{-1} was associated with the ABS buffer's contribution. Moreover, the PMS decomposition rate was basically the same in the presence and absence of BPA, confirming that PMS was decomposed after being activated by Cu-N_4/C-B. Therefore, the degradation of BPA in Cu-N_4/C-B/PMS system displayed a nonradical pathway based on high-valent copper formation (*SI Appendix*, Fig. S31). First, PMS was adsorbed and activated on Cu sites, forming Cu(III)-OH intermediate. Subsequently, the pollutant BPA was adsorbed and attacked by the reactive complex. Afterward, Cu-N_4 sites were reactivated after the desorption of the oxidized BPA.

Theoretical Study of Electronic Structure of Cu SACs. To gain a fundamental understanding of the heteroatom-doped engineering effect on Cu-N_4 SACs, density functional theory (DFT)

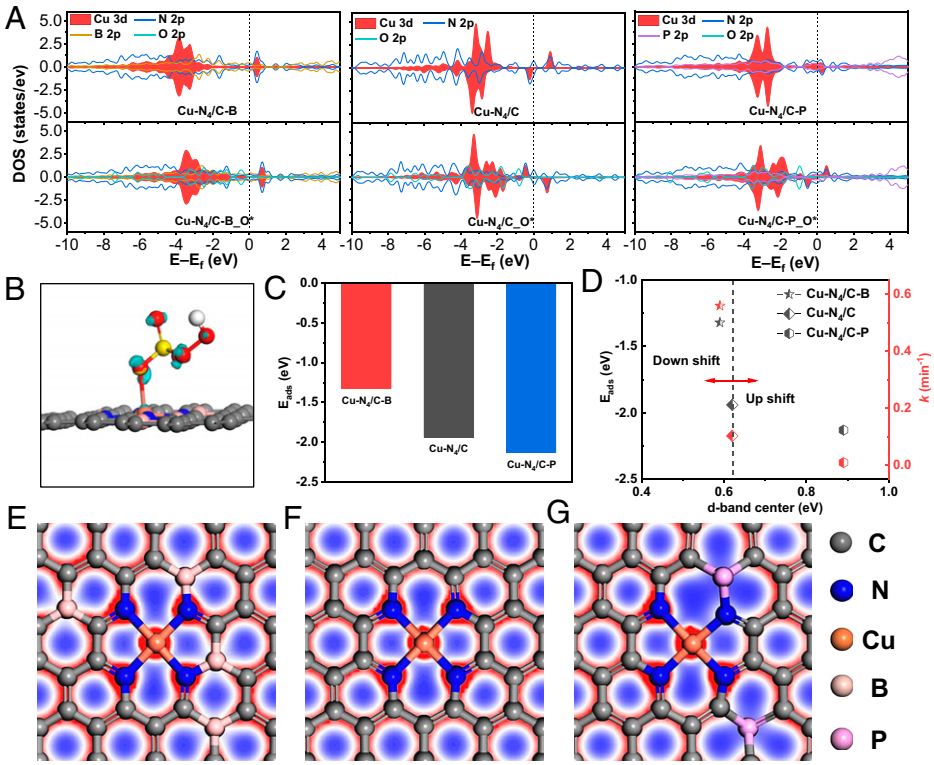

Fig. 4. PDOS and charge density differences analyses. (*A*) PDOS of Cu atom, heteroatoms in the substrate, and oxygen of PMS adsorbed on the Cu center (EF is marked in each graph with the black dashed line). (*B*) The calculated electron density difference diagrams of Cu-N_4/C-B with PMS adsorbed on the Cu-N_4 site. (*C*) The adsorption energy values of PMS on Cu-N_4/C-B, Cu-N_4/C and Cu-N_4/C-P catalysts. (*D*) Relationship between the d-band center and adsorption energy and reaction rate constant for three Cu-N_4 samples. (*E–G*) The optimized structure and the corresponding electron density plots of Cu-N_4/C-B, Cu-N_4/C, and Cu-N_4/C-P catalysts.

calculations were performed to shed light on regulating the electronic structure of Cu active sites for PMS activation. As shown in Fig. 4*A*, the PDOS for the Cu centers, heteroatoms in the substrate and oxygen of PMS adsorbed on the Cu sites were calculated. In apparent contrast to primary Cu-N_4/C, the PDOS of Cu sites in Cu-N_4/C-B displays a negative shift, indicating a decrease in d-band center. Comparatively, the PDOS of Cu atoms in Cu-N_4/C-P moves toward the opposite direction, with an increased d-band center (*SI Appendix*, Fig. S33). Additionally, the PDOS for PMS adsorbed on Cu centers of the three SACs shows that Cu-N_4/C-B has a relatively weak interaction with PMS compared to Cu-N_4/C (*SI Appendix*, Fig. S35). On the contrary, the interaction between Cu-N_4/C-P and PMS is pretty strong. As evidenced from the charge density analysis (Fig. 4*B* and *SI Appendix*, Fig. S36), electron transfer between PMS and Cu-N_4 is observed, suggesting the chemisorption of PMS on all the Cu SACs.

The corresponding adsorption energies (E_{ads}) were further calculated, as shown in Fig. 4*C*. Consistent with the PDOS analysis, Cu-N_4/C-B possesses a small adsorption energy, while Cu-N_4/C and Cu-N_4/C-P display strong binding for PMS. It is inferred that Cu-N_4/C-B catalyst corresponds to a moderate adsorption energy for PMS activation, which results in its superior Fenton-like activity (Fig. 4*D*). On the other hand, both Cu-N_4/C and Cu-N_4/C-P might cause poison of the active sites. Moreover, Bader charge analysis (Fig. 4 *E–G*) shows that the incorporation of heteroatoms has appreciable influence on electron distribution, especially for the Cu centers. As revealed in *SI Appendix*, Fig. S37, the calculated Cu valence state in Cu-N_4/C-B increases markedly in contrast to that of Cu-N_4/C, while Cu-N_4/C-P displays the opposite behavior. The trend of Cu valence state is qualitatively consistent with the XANES and XPS results. Therefore, heteroatom functionalization can serve as an effective strategy to optimize the electronic structure of Cu-N_4 sites, boosting the activation of PMS.

Conclusions

In summary, we systematically investigated the modulation of the electronic structure of Cu-N_4 catalytic sites by heteroatom-doped engineering for Fenton-like oxidation at the atomic level. A series of atomically dispersed Cu-N_4 catalysts were successfully prepared by a hydrogen-bonding-assisted pyrolysis strategy. Both DFT calculations and experimental investigations indicate that the electronic density of the active Cu centers is well controlled via the long-range interaction with heteroatoms. The modified catalyst can readily achieve high improvement of PMS activation kinetics. Importantly, the electron-depleted Cu-N_4/C-B catalyst induces optimized adsorption energy for PMS with an increase of oxidation activity, whereas electron-rich Cu-N_4/C and Cu-N_4/C-P display strong binding of PMS, causing the poison of active sites. This work would provide a deep insight into the electronic structure regulation of metal centers and structure–activity relationship at the atomic level, which could be helpful to develop advanced Fenton-like catalysts.

Materials and Methods

Materials. Copper (II) acetate [$Cu(OAc)_2$], 2,2′:6′,2″-terpyridine, boric acid, phosphoric acid, glucose, and urea were purchased from Sinopharm Chemical Reagent Beijing Co., Ltd. BPA and polyether F127 were obtained from Sigma-Aldrich Chemical Co., Ltd. $KHSO_5{\cdot}0.5KHSO_4{\cdot}0.5K_2SO_4$ (PMS), 5,5-dimethyl-1-pyrroline-*N*-oxide (DMPO), and 2,2,6,6-tetramethyl-4-piperidinol (TMP) were bought from Alfa Aesar Co. Inc. All the chemical reagents were used as received without any other purification.

Synthesis of Cu-N_4/C-B Catalysts. In a typical synthesis of Cu-N_4/C-B catalyst, first the Cu precursor was prepared by mixing $Cu(OAc)_2$ (1 mmol) and 2,2′:6′,2″-terpyridine (1 mmol) in 10 mL of tetrahydrofuran under stirring for 24 h. The resultant precipitate was centrifuged, washed, and vacuum-dried. Subsequently, 50 mmol of carbamide and 1.6 mmol of boric acid were dispersed in 10 mL deionized (DI) water under ultrasonication for 15 min. Then, 0.034 mmol of Cu-contained precursor and 2 mmol of F127 in ethanol (10 mL) were injected into the above solution and the resulting mixture was stirred for 4 h. Then, the H-bonded assemblies were obtained by rotary evaporation of the solvent. Afterward, the sample were pyrolyzed in the Ar atmosphere, maintaining 800 °C for 2 h at a heating rate of 5 °C/min. After being naturally cooled to room temperature, a black powder sample can be obtained. The Cu SACs with B content gradient were prepared by a similar procedure except for changing the amount of boric acid to 0.8 and 2.4 mmol. They are denoted as Cu-N_4/C-B-0.8 and Cu-N_4/C-B-2.4, respectively.

Synthesis of BCN. For the BCN catalyst preparation, 50 mmol of carbamide and 1.6 mmol of boric acid were dispersed in 10 mL DI water under ultrasonication for 15 min, then 2 mmol of F127 in ethanol (10 mL) were injected into the above solution and the resulting mixture was stirred for 4 h. Then, the H-bonded assemblies were obtained by rotary evaporation of the solvent. Afterward, the sample was pyrolyzed in the Ar atmosphere, maintaining 800 °C for 2 h at a heating rate of 5 °C/min. After being naturally cooled to room temperature, a black powder sample can be obtained.

Synthesis of Cu-N_4/C Catalysts. Typically, for the synthesis of Cu-N_4/C catalyst, 50 mmol of carbamide and 0.56 mmol glucose were dispersed in 10 mL DI water under ultrasonication for 15 min. Then, 0.034 mmol of Cu-contained precursor and 2 mmol of F127 in ethanol (10 mL) were injected into the above solution and the resulting mixture was stirred for 4 h. Then, the H-bonded assemblies were obtained by rotary evaporation of the solvent. Afterward, the sample were pyrolyzed in the Ar atmosphere, maintaining 800 °C for 2 h at a heating rate of 5 °C/min. After being naturally cooled to room temperature, a black powder sample can be obtained.

Synthesis of Cu-N_4/C-P Catalysts. In brief, for the synthesis of Cu-N_4/C-P catalyst, 50 mmol of carbamide and 100 μL (1.6 mmol) phosphoric acid were dispersed in 10 mL DI water under ultrasonication for 15 min. Then, 0.034 mmol of Cu-contained precursor and 2 mmol of F127 in ethanol (10 mL) were injected into the above solution and the resulting mixture was stirred for 4 h. Then, the H-bonded assemblies were obtained by rotary evaporation of the solvent. Afterward, the sample were pyrolyzed in the Ar atmosphere, maintaining 800 °C for 2 h at a heating rate of 5 °C/min. After being naturally cooled to room temperature, a black powder sample can be obtained. The Cu SACs with P content gradient were prepared by a similar procedure except for changing the amount of phosphoric acid to 0.8 and 2.4 mmol. They are denoted as Cu-N_4/C-P-0.8 and Cu-N_4/C-P-2.4, respectively.

Synthesis of PCN. For the PCN catalyst preparation, 50 mmol of carbamide and 100 μL phosphoric acid were dispersed in 10 mL DI water under ultrasonication for 15 min, then 2 mmol of F127 in ethanol (10 mL) were injected into the above solution and the resulting mixture was stirred for 4 h. Then, the H-bonded assemblies were obtained by rotary evaporation of the solvent. Afterward, the sample were pyrolyzed in the Ar atmosphere, maintaining 800 °C for 2 h at a heating rate of 5 °C/min. After being naturally cooled to room temperature, a black powder sample can be obtained.

Data Availability. All study data are included in the article and/or *SI Appendix*.

ACKNOWLEDGMENTS. This work was supported by China Ministry of Science and Technology (2021YFA1600800), the National Natural Science Foundation of China (202074104, 51821006, and 52100195), the National Program for Support of Top-Notch Young Professionals, the DNL Cooperation Fund, Chinese Academy of Sciences (CAS) (DNL201918), the Fundamental Research Funds for the Central Universities (WK2060120004, WK2060000021, WK2060000025, and KY2060000180), the CAS Fujian Institute of Innovation, and the DNL201918 Cooperation Fund. This work was partially carried out at the USTC Center for Micro and Nanoscale Research and Fabrication. We acknowledge the Experimental Center of Engineering and Material Science in the University of Science and Technology of China. We thank the photoemission end stations BL1W1B in the Beijing Synchrotron Radiation Facility, BL14W1 in the Shanghai Synchrotron Radiation Facility, and BL10B and BL11U in the National Synchrotron Radiation Laboratory for help with characterizations.

1. D. Jassby, T. Y. Cath, H. Buisson, The role of nanotechnology in industrial water treatment. *Nat. Nanotechnol.* **13**, 670–672 (2018).
2. P. Westerhoff, T. Boyer, K. Linden, Emerging water technologies: Global pressures force innovation toward drinking water availability and quality. *Acc. Chem. Res.* **52**, 1146–1147 (2019).
3. J. Wang, S. Li, Q. Qin, C. Peng, Sustainable and feasible reagent-free electro-Fenton via sequential dual-cathode electrocatalysis. *Proc. Natl. Acad. Sci. U.S.A.* **118**, e2108573118 (2021).
4. Z. Yang, J. Qian, A. Yu, B. Pan, Singlet oxygen mediated iron-based Fenton-like catalysis under nanoconfinement. *Proc. Natl. Acad. Sci. U.S.A.* **116**, 6659–6664 (2019).
5. Z.-Y. Guo *et al.*, Mn−O covalency governs the intrinsic activity of Co-Mn spinel oxides for boosted peroxymonosulfate activation. *Angew. Chem. Int. Ed. Engl.* **60**, 274–280 (2021).
6. A. Jawad *et al.*, Tuning of persulfate activation from a free radical to a nonradical pathway through the incorporation of non-redox magnesium oxide. *Environ. Sci. Technol.* **54**, 2476–2488 (2020).
7. L. Wang *et al.*, Trace cupric species triggered decomposition of peroxymonosulfate and degradation of organic pollutants: Cu(III) being the primary and selective intermediate oxidant. *Environ. Sci. Technol.* **54**, 4686–4694 (2020).
8. G. P. Anipsitakis, D. D. Dionysiou, Radical generation by the interaction of transition metals with common oxidants. *Environ. Sci. Technol.* **38**, 3705–3712 (2004).
9. J. Wang, S. Wang, Activation of persulfate (PS) and peroxymonosulfate (PMS) and application for the degradation of emerging contaminants. *Chem. Eng. J.* **334**, 1502–1517 (2018).
10. P. Hu, M. Long, Cobalt-catalyzed sulfate radical-based advanced oxidation: A review on heterogeneous catalysts and applications. *Appl. Catal. B* **181**, 103–117 (2016).
11. L. W. Matzek, K. E. Carter, Activated persulfate for organic chemical degradation: A review. *Chemosphere* **151**, 178–188 (2016).
12. S. Wacławek *et al.*, Chemistry of persulfates in water and wastewater treatment: A review. *Chem. Eng. J.* **330**, 44–62 (2017).
13. G. P. Anipsitakis, E. Stathatos, D. D. Dionysiou, Heterogeneous activation of oxone using Co_3O_4. *J. Phys. Chem. B* **109**, 13052–13055 (2005).
14. T. Zhang, H. Zhu, J.-P. Croué, Production of sulfate radical from peroxymonosulfate induced by a magnetically separable $CuFe_2O_4$ spinel in water: Efficiency, stability, and mechanism. *Environ. Sci. Technol.* **47**, 2784–2791 (2013).
15. X. Li, A. I. Rykov, B. Zhang, Y. Zhang, J. Wang, Graphene encapsulated Fe_xCo_y nanocages derived from metal–organic frameworks as efficient activators for peroxymonosulfate. *Catal. Sci. Technol.* **6**, 7486–7494 (2016).
16. S. Yang *et al.*, MOF-templated synthesis of $CoFe_2O_4$ nanocrystals and its coupling with peroxymonosulfate for degradation of bisphenol A. *Chem. Eng. J.* **353**, 329–339 (2018).
17. E.-T. Yun, J. H. Lee, J. Kim, H.-D. Park, J. Lee, Identifying the nonradical mechanism in the peroxymonosulfate activation process: Singlet oxygenation versus mediated electron transfer. *Environ. Sci. Technol.* **52**, 7032–7042 (2018).
18. X. Duan, H. Sun, Y. Wang, J. Kang, S. Wang, N-doping-induced nonradical reaction on single-walled carbon nanotubes for catalytic phenol oxidation. *ACS Catal.* **5**, 553–559 (2015).
19. G. C. Bond, The origins of particle size effects in heterogeneous catalysis. *Surf. Sci.* **156**, 966–981 (1985).
20. L. Liu, A. Corma, Metal catalysts for heterogeneous catalysis: From single atoms to nanoclusters and nanoparticles. *Chem. Rev.* **118**, 4981–5079 (2018).
21. X. Zheng *et al.*, Origin of enhanced water oxidation activity in an iridium single atom anchored on NiFe oxyhydroxide catalyst. *Proc. Natl. Acad. Sci. U.S.A.* **118**, e2101817118 (2021).
22. Y. Shang, X. Xu, B. Gao, S. Wang, X. Duan, Single-atom catalysis in advanced oxidation processes for environmental remediation. *Chem. Soc. Rev.* **50**, 5281–5322 (2021).
23. Z. Li *et al.*, Activation of peroxymonosulfate by iron-biochar composites: Comparison of nanoscale Fe with single-atom Fe. *J. Colloid Interface Sci.* **582** (Pt B), 598–609 (2021).
24. X. Li *et al.*, Single cobalt atoms anchored on porous N-doped graphene with dual reaction sites for efficient fenton-like catalysis. *J. Am. Chem. Soc.* **140**, 12469–12475 (2018).
25. X. Mi *et al.*, Almost 100 % peroxymonosulfate conversion to singlet oxygen on single-atom CoN_{2+2} sites. *Angew. Chem. Int. Ed. Engl.* **60**, 4588–4593 (2021).
26. J. A. Zamora Zeledón *et al.*, Tuning the electronic structure of Ag-Pd alloys to enhance performance for alkaline oxygen reduction. *Nat. Commun.* **12**, 620 (2021).
27. J. Wang *et al.*, Heteroatom-doping of non-noble metal-based catalysts for electrocatalytic hydrogen evolution: An electronic structure tuning strategy. *Small Methods* **5**, e2000988 (2021).
28. J. Wan *et al.*, In situ phosphatizing of triphenylphosphine encapsulated within metal–organic frameworks to design atomic Co_1–P_1N_3 interfacial structure for promoting catalytic performance. *J. Am. Chem. Soc.* **142**, 8431–8439 (2020).
29. Y. Wang *et al.*, High-efficiency oxygen reduction to hydrogen peroxide catalyzed by nickel single-atom catalysts with tetradentate N_2O_2 coordination in a three-phase flow cell. *Angew. Chem. Int. Ed. Engl.* **59**, 13057–13062 (2020).
30. H. Shen *et al.*, Synergistic effects between atomically dispersed Fe−N−C and C−S−C for the oxygen reduction reaction in acidic media. *Angew. Chem. Int. Ed. Engl.* **56**, 13800–13804 (2017).
31. Y. Mun *et al.*, Versatile strategy for tuning ORR activity of a single Fe-N_4 site by controlling electron-withdrawing/donating properties of a carbon plane. *J. Am. Chem. Soc.* **141**, 6254–6262 (2019).

32. H. Wu *et al.*, Regulating the allocation of N and P in codoped graphene via supramolecular control to remarkably boost hydrogen evolution. *Energy Environ. Sci.* **12**, 2697–2705 (2019).
33. Y. Zheng *et al.*, Toward design of synergistically active carbon-based catalysts for electrocatalytic hydrogen evolution. *ACS Nano* **8**, 5290–5296 (2014).
34. Y. Zhao *et al.*, Can boron and nitrogen co-doping improve oxygen reduction reaction activity of carbon nanotubes? *J. Am. Chem. Soc.* **135**, 1201–1204 (2013).
35. H. L. Poh, M. Pumera, *p*-Element-doped graphene: Heteroatoms for electrochemical enhancement. *ChemElectroChem* **2**, 190–199 (2015).
36. H. B. Yang *et al.*, Atomically dispersed Ni(I) as the active site for electrochemical CO_2 reduction. *Nat. Energy* **3**, 140–147 (2018).
37. F. Li *et al.*, Boosting oxygen reduction catalysis with abundant copper single atom active sites. *Energy Environ. Sci.* **11**, 2263–2269 (2018).
38. C. Zhao *et al.*, Solid-diffusion synthesis of single-atom catalysts directly from bulk metal for efficient CO_2 reduction. *Joule* **3**, 584–594 (2019).
39. R. Golnak *et al.*, Intermolecular bonding of hemin in solution and in solid state probed by N K-edge X-ray spectroscopies. *Phys. Chem. Chem. Phys.* **17**, 29000–29006 (2015).
40. H. C. Choi *et al.*, X-ray absorption near edge structure study of BN nanotubes and nanothorns. *J. Phys. Chem. B* **109**, 7007–7011 (2005).
41. W. Liu *et al.*, Discriminating catalytically active FeN_x species of atomically dispersed Fe–N–C catalyst for selective oxidation of the C–H bond. *J. Am. Chem. Soc.* **139**, 10790–10798 (2017).
42. H. Shang *et al.*, Engineering unsymmetrically coordinated $Cu\text{-}S_1N_3$ single atom sites with enhanced oxygen reduction activity. *Nat. Commun.* **11**, 3049 (2020).
43. Y. Zhou *et al.*, Activation of peroxymonosulfate by benzoquinone: A novel nonradical oxidation process. *Environ. Sci. Technol.* **49**, 12941–12950 (2015).
44. T. Zhang *et al.*, Efficient peroxydisulfate activation process not relying on sulfate radical generation for water pollutant degradation. *Environ. Sci. Technol.* **48**, 5868–5875 (2014).
45. G. Yu, Y. Wang, H. Cao, H. Zhao, Y. Xie, Reactive oxygen species and catalytic active sites in heterogeneous catalytic ozonation for water purification. *Environ. Sci. Technol.* **54**, 5931–5946 (2020).
46. L. Ge, J. Chen, X. Qiao, J. Lin, X. Cai, Light-source-dependent effects of main water constituents on photodegradation of phenicol antibiotics: Mechanism and kinetics. *Environ. Sci. Technol.* **43**, 3101–3107 (2009).
47. A. A. Gorman, M. A. J. Rodgers, Singlet molecular oxygen. *Chem. Soc. Rev.* **10**, 205–231 (1981).
48. Y. Gao, Z. Chen, Y. Zhu, T. Li, C. Hu, New insights into the generation of singlet oxygen in the metal-free peroxymonosulfate activation process: Important role of electron-deficient carbon atoms. *Environ. Sci. Technol.* **54**, 1232–1241 (2020).
49. J. Lee, U. von Gunten, J.-H. Kim, Persulfate-based advanced oxidation: Critical assessment of opportunities and roadblocks. *Environ. Sci. Technol.* **54**, 3064–3081 (2020).
50. X. Duan, H. Sun, Z. Shao, S. Wang, Nonradical reactions in environmental remediation processes: Uncertainty and challenges. *Appl. Catal. B* **224**, 973–982 (2018).
51. K. Z. Huang, H. Zhang, Direct electron-transfer-based peroxymonosulfate activation by iron-doped manganese oxide (δ-MnO_2) and the development of galvanic oxidation processes (GOPs). *Environ. Sci. Technol.* **53**, 12610–12620 (2019).
52. Y. Wang *et al.*, Insights into the generation of high-valent copper-oxo species in ligand-modulated catalytic system for oxidizing organic pollutants. *Chem. Eng. J.* **304**, 1000–1008 (2016).
53. J. G. McAlpin *et al.*, Electronic structure description of a $[Co(III)_3Co(IV)O_4]$ cluster: A model for the paramagnetic intermediate in cobalt-catalyzed water oxidation. *J. Am. Chem. Soc.* **133**, 15444–15452 (2011).
54. Y. Deng, A. D. Handoko, Y. Du, S. Xi, B. S. Yeo, In situ Raman spectroscopy of copper and copper oxide surfaces during electrochemical oxygen evolution reaction: Identification of Cu^{III} oxides as catalytically active species. *ACS Catal.* **6**, 2473–2481 (2016).